Applied Science and Engineering Progress, Vol. 20, No. 4, 2027, 8388

Research Article

Experimental and DFT Investigation of Fe-Modified TiO_2-MoO_3 Heterostructures for Microwave Absorption

Ahmad Fajrin Kusuma Wijaya*, Purnomo Yusgiantoro, Muhammad Sidik Boedoyo, and Mitro Prihantoro
Department of Defense Technology, Indonesia Defense University, Bogor, Indonesia

* Corresponding author. E-mail: fajrin.wijaya@doktoral.idu.ac.id DOI: 10.14416/j.asep.2026.11.009
Received: 25 August 2026; Revised: 27 September 2026; Accepted: 19 October 2026; Published online: 20 November 2026
© 2026 King Mongkut's University of Technology North Bangkok. All Rights Reserved

Abstract
The proliferation of high-frequency radar systems and electromagnetic interference (EMI) has created a growing need for highly efficient broadband radar-absorbing materials (RAM). This study investigates the dual-loss attenuation mechanisms of a novel Fe-doped Ti–Mo oxide heterostructure through experimental synthesis and density functional theory (DFT) calculations. X-ray diffraction (XRD) confirmed the successful synthesis of the composite, revealing the coexistence of anatase TiO_2 and α-MoO_3 phases and providing a structural basis for investigating the incorporation of dilute Fe dopants. Although macroscopic reflection loss (RL) profiles remain to be experimentally validated using a vector network analyzer (VNA), first-principles DFT calculations based on a 180-atom supercell elucidated the underlying theoretical mechanisms that may contribute to synergistic microwave absorption. The calculated density of states for the composite crosses the Fermi level, while the calculated work function is 8.15 eV, suggesting the potential for enhanced dielectric loss through interfacial charge redistribution analogous to a nanocapacitor mechanism. Meanwhile, Fe dopants act as localized magnetic centers, inducing spin polarization and ferrimagnetic-like alignment, with a total magnetic moment of 17.0 μB per 180-atom supercell. These findings suggest the potential for p–d superexchange interactions to facilitate energy dissipation through magnetic loss. Furthermore, the calculated d-band centers exhibit a distinct hierarchy, with Ti (−0.48 eV) potentially facilitating electron mobility, Fe (−1.71 eV) contributing to magnetic localization, and Mo (−1.84 eV) participating in p–d orbital hybridization associated with the structural stability of the theoretical model. Overall, this study highlights the potential roles of atomic-scale interfacial engineering and defect-induced spin polarization in microwave attenuation, establishing a theoretical framework for the future experimental development of broadband radar-absorbing materials.

Keywords: d-band center, Density functional theory, Ferrimagnetism, Heterostructure, Interfacial polarization, Radar absorbing material

1 Introduction

The rapid development of high-frequency telecommunications technology and modern radar systems has triggered a surge in electromagnetic interference (EMI) pollution [1]–[3]. Uncontrolled exposure to electromagnetic radiation not only disrupts the functionality of sensitive electronic instruments but also poses a serious threat to the security of sensitive aerospace electronic systems [4]–[6]. Therefore, developing high-performance Radar Absorbing Materials (RAM) that dissipate microwave energy as thermal energy has become one of the most crucial research focuses in materials science [7], [8]. The ideal RAM must meet strict criteria, namely a thin profile, light weight, broadband absorption, and strong attenuation capacity [9]–[11].

Fundamentally, the absorption performance of electromagnetic waves is controlled by the synergy between dielectric loss and magnetic loss [12]. Conventional absorbing materials often fail to meet these ideal criteria due to intrinsic imbalances. For example, although carbon-based materials (such as graphene or carbon nanotubes) possess substantial dielectric loss, they exhibit excessive electrical conductivity and almost no magnetic loss. This imbalance leads to a severe impedance mismatch that reflects incident waves into the air rather than allowing them to penetrate and be absorbed [13]–[15]. In contrast, while traditional bulk ferrite materials

Applied Science and Engineering Progress, Vol. 20, No. 4, 2027, 8388

provide excellent magnetic losses, their practical application is often constrained by high physical density and inherently limited dielectric loss [16]. It is important to acknowledge, however, that these limitations are not absolute; the electromagnetic performance of ferrites is highly tunable and strongly dependent on their specific chemical composition, structural morphology, filler loading fraction, and the target frequency band. Therefore, the most rational strategy to address this impedance dilemma is to design heterostructure composite materials that blend conductive dielectric components with magnetic attenuation centers in a single-phase architecture [17], [18].

Transition metal oxides (TMOs) have emerged as promising RAM candidates because of their rich valence states and ease of engineering structural defects [19]–[22]. In this context, Titanium dioxide (TiO_2) is widely recognized as a robust base material with excellent dielectric polarizability for microwave absorption applications [23], [24], while Molybdenum trioxide (α-MoO_3) offers a unique layered (2D) crystal structure with high interfacial reactivity. The formation of TiO_2/α-MoO_3 heterostructures is believed to trigger significant interfacial polarization effects [25]–[28]. Furthermore, to introduce magnetic loss properties absent in both oxides, the defect-engineering strategy of inserting (doping) magnetic transition-metal atoms, such as Iron (Fe), is a highly strategic approach. Introducing Fe dopants not only induces a local magnetic dipole network to attenuate high-frequency signals, but also creates a local coordination environment that structurally and energetically facilitates the dissociation of surface hydroxyls (forming active defect sites). These vacancy defects act as active electron traps, significantly amplifying dielectric loss via localized dipole polarization. However, such active defect sites are conventionally highly vulnerable to environmental degradation, particularly "water poisoning" in humid or marine operational conditions [19], [29].

Nevertheless, although researchers have widely synthesized experimentally doped oxide composites, the fundamental understanding of the wave-absorption mechanism and environmental stability at the atomic level remains elusive. Most current literature evaluates macroscopic performance solely using Vector Network Analyzer (VNA) parameters to derive complex permittivity/permeability and Reflection Loss (RL). While VNA measurements are the absolute empirical standard for defining final macroscopic RAM performance, relying solely on them leaves the fundamental atomic-level wave-absorption mechanisms largely unresolved. Therefore, rather than reporting macroscopic RL curves, this study focuses entirely on unraveling the intrinsic quantum-mechanical origins of these losses. Comprehensive investigations of interfacial charge-transfer dynamics, the d-band center hierarchy, spin-exchange interactions, and the thermodynamics of microsolvation by environmental moisture are rarely reported [30]–[32].

Building on this knowledge gap, this study reports the experimental fabrication and a comprehensive quantum-mechanical investigation of Fe-doped Ti-Mo oxide heterostructures. The composite powders were synthesized via coprecipitation, and phase purity was confirmed by X-ray diffraction (XRD). To elucidate the attenuation mechanism, Density Functional Theory (DFT)-based first-principles modeling was performed on a 180-atom supercell. Advanced calculations, including d-band center analysis, Electron Localization Function (ELF) topology, work-function potential mapping, and ferrimagnetic spin density extraction, were performed. Furthermore, a microsolvation thermodynamic model using a $(H_2O)_3$ trimer was applied to validate the material's structural stability and localized resistance to moisture-induced defect passivation. This combination of experimental and theoretical methods is expected to push the boundaries of current microwave-absorbing material design while providing a fundamental blueprint for developing next-generation radar-absorbing materials.

2 Materials and Methods

2.1 *Materials*

All chemicals used in this study were of analytical grade and used directly without further purification. The metal precursors of the composite matrix include Titanium tetrachloride ($TiCl_4$), Ammonium heptamolybdate tetrahydrate ($(NH_4)_6Mo_7O_{24}\cdot 4H_2O$), and Iron(III) nitrate nonahydrate ($Fe(NO_3)_3\cdot 9H_2O$). Ammonia solution (NH_4OH) was used as a precipitating agent to control the acidity (pH) of the reaction system, while deionized water served as the universal solvent.

Applied Science and Engineering Progress, Vol. 20, No. 4, 2027, 8388

2.2 *Synthesis of Fe-Doped Ti-Mo oxide heterostructures*

Wave-absorbing composites were synthesized via a controlled coprecipitation method. Typically, the metal precursors were dissolved in 100 mL of deionized water to form a 0.1 M precursor solution. The solution was subjected to continuous magnetic stirring at 500 rpm for 3 hours at room temperature to achieve homogeneous molecular mixing. The precursor stoichiometric molar ratio of $TiCl_4$: $Fe(NO_3)_3 \cdot 9H_2O$: $(NH_4)_6Mo_7O_{24} \cdot 4H_2O$ was strictly maintained at 7: 0.14: 1. This specific stoichiometry yields an equimolar atomic ratio of Ti and Mo (1:1) while establishing a highly dilute Fe dopant concentration of approximately 1.0 atomic percent, which directly correlates with the ~0.55 at% Fe concentration modeled in the 180-atom DFT supercell.

The precipitation process was induced by the dropwise addition (approximately 2 mL/min) of NH_4OH solution under constant stirring until the system reached a stable pH of 9.0, resulting in a homogeneous suspension. The reaction system was then heated to 80°C and aged for 2 hours to facilitate nucleation and phase maturation. The resulting solid precipitate was isolated via vacuum filtration and rigorously washed three times with deionized water and twice with absolute ethanol to remove residual chloride and nitrate ions. The purified precipitate was dried in an ambient air oven at 110°C for 12 hours. Finally, the dried powder was placed in an alumina crucible and calcined in a muffle furnace at 800°C for 5 hours in an ambient air atmosphere, utilizing a controlled heating and cooling rate of 5°C/min. The final yield of the composite powder was approximately 82%. While this elevated calcination temperature (800°C) inherently promotes some grain growth and reduces the specific interfacial area, it was strictly necessary to provide the substantial thermal activation energy required to force the Fe atoms into substitutional lattice sites (preventing surface segregation) and to achieve the high degree of crystallinity necessary to minimize amorphous electron-scattering defects, thereby optimizing the macroscopic interfacial charge redistribution. It should be explicitly noted that this experimental procedure was conducted as a preliminary proof-of-concept synthesis to establish a qualitative empirical baseline for phase coexistence, rather than a statistically evaluated, fully optimized production protocol.

2.3 *First-principles calculations and computational details*

The electronic structure and magnetic properties of Fe-doped Ti-Mo heterostructures were investigated using density functional theory (DFT) first-principles calculations. All simulation calculations were executed using the open-source software Quantum ESPRESSO. The exchange-correlation interaction between electrons is evaluated using the Generalized Gradient Approximation (GGA) approach with the Perdew-Burke-Ernzerhof (PBE) functional. The interaction between valence electrons and atomic nuclei and their core electrons is modeled using the Projector Augmented-Wave (PAW) pseudopotential [33]–[35].

To ensure the theoretical model accurately reflects the experimentally synthesized material, the large-scale heterostructure supercell (comprising 180 atoms) was constructed by interfacing the specific crystallographic planes identified as dominant in the XRD analysis: namely, the Anatase TiO_2 (101) facet and the α-MoO_3 (010) facet. The interface was constructed with O-terminations to minimize surface energy. A single Iron (Fe) atom was substituted at an octahedral Ti lattice site near the interface, yielding a theoretical dopant concentration of ~0.55 at%, which closely mirrors the dilute empirical target. The simulated lattice parameters of the asymmetric slab were a = 39.18 Å, b = 15.27 Å, and c = 28.65 Å. Standard 3D periodic boundary conditions (PBCs) were applied, explicitly incorporating a 15 Å vacuum layer along the z-direction (c-axis) to prevent non-physical electrostatic interactions between adjacent periodic slab images. Given the large spatial extent of the supercell, the Brillouin zone was effectively sampled using a single Gamma point (Γ) to optimize computational efficiency without sacrificing physical accuracy. The fully relaxed structural coordinates are provided as a supplementary POSCAR/CIF file.

The ion-electron interactions were described using Vanderbilt Ultrasoft Pseudopotentials (USPP) from the Quantum ESPRESSO library, explicitly treating the following valence electron configurations: Ti ($3s^23p^63d^24s^2$), Mo ($4s^24p^64d^55s^1$), Fe ($3s^23p^63d^64s^2$), and O ($2s^22p^4$). Because the USPP framework is specifically designed to operate efficiently at lower energy thresholds, the plane-wave basis set electron wave function expansion was constrained with cutoff

Applied Science and Engineering Progress, Vol. 20, No. 4, 2027, 8388

energy values of 30 Ry for the wave function and 300 Ry for the charge density. Preliminary convergence testing demonstrated that these cutoffs yielded total energy variations of less than 2 meV/atom. Furthermore, because the supercell possesses large spatial dimensions (up to ~39.18 Å), the corresponding reciprocal Brillouin zone is infinitesimally small. Therefore, sampling restricted to a single Gamma point (Γ) is mathematically equivalent to a highly dense k-point mesh in a primitive unit cell, guaranteeing high computational accuracy.

To account for the high density of states near the Fermi level and the metallic nature of the highly doped interface, Marzari-Vanderbilt cold smearing with a broadening parameter of 0.01 Ry was employed to secure stable Self-Consistent Field (SCF) electronic convergence. During the structural geometry optimization, the bottom two atomic layers of the TiO_2 matrix were fixed to their bulk lattice coordinates to accurately mimic the semi-infinite bulk constraint, while the upper TiO_2 layers, the Fe dopant, and the entire α-MoO_3 interface were permitted to fully relax until the Hellmann-Feynman forces acting on each freely moving atom were minimized below 10^{-3} Ry/Bohr. Additionally, to compensate for the asymmetric nature of the heterostructure slab along the c-axis, an artificial macroscopic dipole correction was explicitly applied along the z-direction, ensuring a highly accurate evaluation of the electrostatic vacuum potential [36].

It is well-documented that the standard PBE exchange-correlation functional tends to underestimate the bandgap of strongly correlated transition-metal oxides due to inherent self-interaction errors, which can artificially delocalize 3d electrons. While applying a Hubbard correction (DFT+U) is often utilized to rectify absolute bandgap values, standard PBE was deliberately retained for this specific study. In a highly asymmetric ternary heterostructure (involving Fe, Ti, and Mo), applying empirical U parameters can inadvertently introduce artificial energetic biases across the interface, potentially distorting the delicate macroscopic charge transfer dynamics and spontaneous p-d hybridization. Therefore, the uncorrected PBE framework was employed to provide a mathematically unbiased, systematically consistent baseline for tracing relative interfacial charge redistribution, spatial superexchange networks, and structural thermodynamics, rather than determining exact macroscopic optical bandgaps.

All calculations were performed with the spin-polarization parameter enabled to capture the material's intrinsic magnetic moment. Further analysis of the Total Density of States (TDOS) and Projected Density of States (PDOS) was performed using the Gaussian smearing method with a degauss value of 0.02 Ry to produce a representative energy curve profile [37].

To unravel the physical mechanism at the heterostructure interface, a series of post-processing calculations was comprehensively performed. Local charge distributions and transfers, along with absolute magnetic moment values, were evaluated using Löwdin population analysis. Chemical bond topology and orbital hybridization were visualized through Electron Localization Function (ELF) extraction [38]. Meanwhile, planar and macroscopic electrostatic potential profiles were extracted along the z-axis (perpendicular to the interface) to determine the material's work function. Furthermore, the position of the d-band center is theoretically calculated by numerically integrating the first moment of the PDOS curve, using integration constraints parallel to the Fermi level.

2.4 *Thermodynamic and micro-solvation cluster modeling*

To precisely evaluate the local thermodynamics of oxygen vacancy formation (E_{vac}) and the micro-solvation interactions with environmental moisture, localized molecular cluster models were investigated. These specific quantum-chemical calculations were performed using the ORCA program package. The geometry optimizations and thermodynamic evaluations were performed utilizing the hybrid Becke, 3-parameter, Lee-Yang-Parr (B3LYP) exchange-correlation functional [39]. To accurately capture long-range non-covalent interactions and van der Waals forces during the micro-solvation process, Grimme's empirical dispersion correction with Becke-Johnson damping (D3BJ) was explicitly incorporated. This dispersion-corrected framework was utilized in conjunction with the def2-SVP basis set. To reduce computational cost in evaluating Coulomb terms, the Resolution of Identity chain-of-spheres (RIJCOSX) approximation was used with the auxiliary def2/J basis set. To construct the molecular cluster models, representative local coordination spheres were excised from the relaxed periodic heterostructure lattice. All truncated boundary bonds were saturated with Hydrogen atoms (H-termination) to prevent artificial electronic polarization from dangling bonds. Because active macroscopic oxide surfaces in ambient

Applied Science and Engineering Progress, Vol. 20, No. 4, 2027, 8388

environments are typically hydrated, the pristine cluster was explicitly modeled as a neutral, H-terminated species with active surface hydroxyls. Consequently, the localized defect generation was modeled specifically via the dissociation of a surface hydroxyl group (forming a neutral surface defect), strictly distinguishing it from the removal of a bare bulk lattice oxygen atom. The relative energetic cost for this hydroxyl dissociation (E_{vac}) was mathematically extracted using the reaction equation: $E_{vac} = G_{defect} + G_{OH} - G_{pristine}$, maintaining an overall neutral charge state for the primary cluster system.

Harmonic vibrational frequency calculations were systematically conducted on the optimized geometries to confirm the absence of imaginary frequencies (verifying true local minima) and to extract the final Gibbs Free Energy (G) at standard room temperature (298.15 K). For open-shell systems, specifically the defective Fe clusters and microsolvation interaction complexes containing unpaired electrons, the Unrestricted Kohn-Sham (UKS) formalism was strictly employed, with accurately defined spin multiplicities, to capture spin-polarization effects. Furthermore, to evaluate the structural immunity against water poisoning, a cyclic water trimer $(H_2O)_3$ was constructed as a micro-droplet model to calculate the physical adsorption energy (E_{ads}) and to visualize the steric repulsion dynamics at the defective Fe site.

3 Results and Discussion

3.1 *Phase composition and crystallographic analysis via XRD*

The successful synthesis of the wave-shielding heterostructure composite was validated experimentally by X-ray diffraction (XRD) analysis. The XRD spectrum (Figure 1) clearly shows characteristic peaks confirming the coexistence of polycrystalline domains of molybdenum trioxide (α-MoO_3) and titanium dioxide (Anatase). It is very important to note that no additional diffraction peaks relating to secondary iron oxide phases (such as FeO or Fe_2O_3) were detected at the resolution limit of the instrument. While the absence of secondary iron-oxide diffraction peaks (such as FeO or Fe_2O_3) within the instrument's resolution limit suggests the successful incorporation of the highly dilute Fe dopant (approximately 1.0 at%) into the host matrix, it does not definitively rule out the possibility of nanoscale segregation or amorphous phase formation. Acknowledging the inherent detection limits of standard benchtop XRD, the absolute confirmation of atomic-level substitution, exact coordination, and Fe oxidation state would require future advanced spectroscopic investigations, such as X-ray Photoelectron Spectroscopy (XPS) or STEM-EDS mapping. Nevertheless, the absence of macroscopic crystalline impurities provides a reasonable and solid empirical baseline that justifies the idealized single-atom substitutional model subsequently employed in the 180-atom DFT supercell. The successful atomic integration of these transition-metal dopants triggers local lattice distortions, strategically designed to serve as active centers for electromagnetic wave absorption.

Furthermore, the diffractogram shows a very strong peak at $2\theta \approx 25.76°$. This very sharp and broad peak profile is the result of intense peak overlap between the main diffraction planes of the anatase TiO_2 phase (101 plane) and the molybdite α-MoO_3 phase (040 plane) [40]–[43]. The close angular position of these two oxide matrices causes the TiO_2 peak to be masked in the diffraction profile. In addition, theappearance of a series of high-intensity diffractionpeaks at 12.8°, 25.7°, and 39.1°, which are characteristic of the (0k0) orientation family, indicates the preferred orientation of crystal growth for the α-MoO_3 phase. This phenomenon proves that the α-MoO_3 phase grows to form a layered structure with a very high degree of crystallinity, while the TiO_2 phase and Fe dopants are homogeneously distributed between them. This composite structure, which combines layered crystalline domains and interfacial heterogeneity, is highly advantageous, as it significantly increases the number of interfacial defects that serve as dielectric polarization centers.

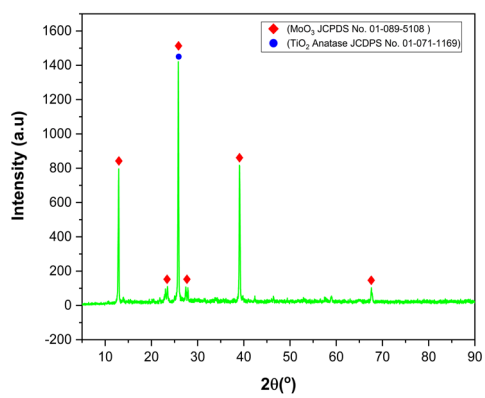


Figure 1: Experimental X-ray diffraction (XRD) pattern of the synthesized composite, revealing the phase coexistence and peak overlapping of Anatase

TiO_2 and α-MoO_3 without secondary iron oxide impurities.

3.2 *Structural configuration and interfacial engineering*

A fundamental step in designing high-performance electromagnetic wave-absorbing materials is controlling the microscopic architecture at the atomic level. Figure 2 shows a relaxed structural model of a Fe-doped Ti-Mo heterostructure supercell containing 180 atoms. Geometrically, the system displays a two-dimensional (2D) heterostructure topology showing a clear interface between the Titanium-based oxide lattice domain (bottom layer) and the Molybdenum oxide cluster/layer (top layer).

The existence of this solid-solid interface is essential to the mechanism of electromagnetic wave attenuation. The difference in work function and electron density between the Ti-O and Mo-O phases results in a significant charge redistribution at the interface. This phenomenon leads to a strong interfacial polarization via interfacial charge redistribution. In Radar Absorbing Material (RAM) applications, the accumulation of dipoles in this interfacial area will respond to the electric field of incident microwaves (radar) in a fluctuating manner, thereby significantly enhancing energy dissipation through dielectric loss. This architectural design aligns well with recent experimental findings on TiO_2/α-MoO_3 heterojunctions [25], [27], [28] and magnetic oxide nanocomposites [16], [17], [24], where constructing a well-defined solid-solid phase boundary was proven to significantly accelerate interfacial charge migration compared to single-phase counterparts.

Furthermore, Figure 2 highlights the defect-engineering strategy through substitutional doping. A single Iron (Fe) atom (represented by a gold/orange colored sphere) was successfully integrated into the Ti-O matrix. This Fe placement intentionally breaks the local crystal symmetry, triggering lattice distortions in its vicinity. This modification of the local coordination environment not only serves as an electron-scattering center to improve microscopic resistance but also acts as the main anchor for local magnetic moment carriers. The presence of magnetic transition-metal (Fe) atoms within this conductive oxide matrix creates a synergistic effect, combining the electrical conductivity of the Ti-Mo-O matrix with the magnetic anisotropy of Fe to produce a dual-loss mechanism ideal for advanced electromagnetic wave-absorbing applications.

3.3 *Electronic structure and wave attenuation mechanism*

Density of States (DOS) evaluation is a fundamental parameter for predicting the feasibility of materials for advanced microwave absorption applications, especially as Radar Absorbing Materials (RAMs) or electromagnetic interference shielding (EMI shielding). Figure 3 represents the TDOS and PDOS spin-polarization profiles of Fe-doped Ti-Mo heterostructures calibrated against the Fermi energy (E_F = 0 eV).

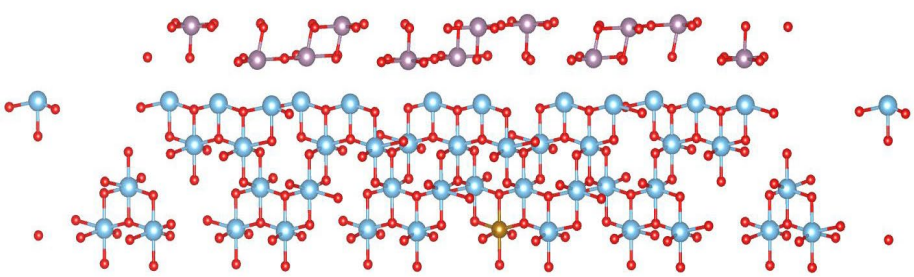


Figure 2: Side-view atomic configuration of the relaxed 180-atom Fe-doped Ti-Mo heterostructure. The model illustrates the interfacial junction between the Titanium-based oxide domain (light blue spheres) and the Molybdenum oxide layer (purple spheres). Red spheres represent Oxygen atoms. The substitutionally doped Iron (Fe) atom, acting as the primary magnetic center, is highlighted in gold/orange.

Applied Science and Engineering Progress, Vol. 20, No. 4, 2027, 8388

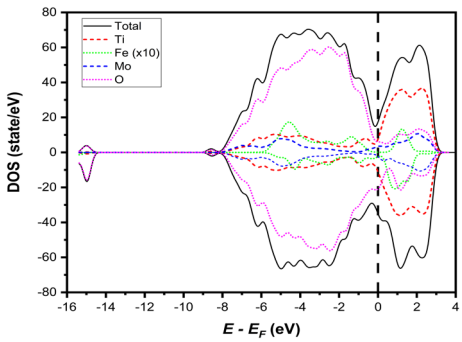


Figure 3: Calculated spin-polarized Total Density of States (TDOS) and element-resolved Projected Density of States (PDOS) for the Fe-doped Ti-Mo heterostructure. The vertical dashed line indicates the Fermi level (EF) set to 0 eV. The PDOS of the Fe atom is magnified by a factor of 10 for clarity.

3.3.1 Density of states and dielectric loss potential

Based on the standard GGA-PBE TDOS profile, the calculated density of states of this material crosses the Fermi level. It is important to acknowledge that standard GGA functionals intrinsically underestimate bandgaps, often artificially projecting zero-gap metallic states for heavily doped transition metal oxides compared to Hubbard-corrected (DFT+U) methods [44], [45].

Nevertheless, the presence of a large valence-electron population near the Fermi level in both majority and minority spin channels definitively confirms the metallic (conductive) behavior of this system. In the context of electromagnetic wave attenuation, this strong metallic nature is a double-edged sword. While the abundance of delocalized free electrons near the Fermi level facilitates high conduction and dielectric loss, excessive macroscopic conductivity typically leads to severe impedance mismatch, causing incident waves to be reflected at the surface rather than absorbed. For an ideal Radar Absorbing Material (RAM), it is fundamentally required that the normalized input impedance (Z_{in}/Z_0) approaches unity to allow wave penetration.

Therefore, it is theoretically hypothesized that while the continuous density of states at the Fermi level provides the necessary charge carriers for internal dielectric dissipation, the extensive integration of structural defects (oxygen vacancies) and highly localized magnetic centers (Fe) is strictly required to modulate this conductivity. This careful balance of dielectric and magnetic properties is theoretically essential to satisfy the impedance matching prerequisite and prevent total reflective loss.

3.3.2 Chemical bonding and thermodynamic stability via p-d hybridization

Defense applications demand materials that are not only electronically functional but also structurally stable under extreme conditions. Analysis of the valence band profile over a deep energy range (-8 eV to -2 eV) shows the absolute dominance of the 2p orbitals of the Oxygen atom, which hybridize strongly with the 3d orbitals of Titanium and the 4d orbitals of Molybdenum.

This overlapping of energy bands is a manifestation of the very strong covalent bonding between oxygen and its constituent transition metals. This extensive p-d hybridization serves as a structural backbone, suggesting that these Fe-doped Ti-Mo heterostructures possess mechanical robustness and thermal stability, making them suitable as robust electromagnetic coating materials.

To directly visualize the chemical bonding strength and mechanical stability of these heterostructures, the Electron Localization Function (ELF) topology was extracted and projected in Figure 4. This ELF mapping is a highly reliable metric for measuring the probability of finding pairs of electrons with opposite spins; values close to the upper limit (ELF ® 1) indicate highly localized electron pairing, which is characteristic of strong covalent interactions.

In the 3D contour map, the formation of very dense electron bridges connecting the transition-metal dopants (Ti, Mo, and Fe) to the surrounding oxygen atoms is clearly observed. This precise charge localization in the interatomic space acts as a direct visual corroboration of the p-d orbital overlap previously identified in the PDOS curves and the charge transfer vectors extracted from the Löwdin population analysis. Together, these multiparameter electronic signatures, localized electron pairing (ELF), orbital hybridization (PDOS), and charge redistribution (Löwdin), confirm the presence of robust covalent bonds. Interestingly, this substantial orbital overlap also indicates a highly stabilized interface between the Titanium and Molybdenum oxide layers. In practical terms, this robust interlayer

Applied Science and Engineering Progress, Vol. 20, No. 4, 2027, 8388

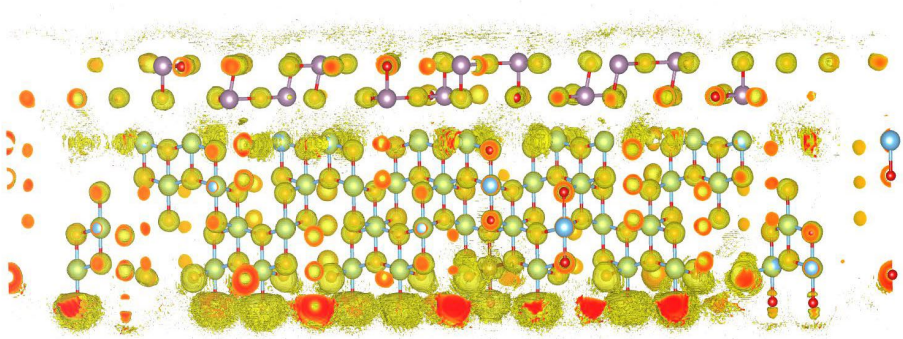


Figure 4: Three-dimensional Electron Localization Function (ELF) contour (isovalue = 0.75) of the Fe-doped Ti-Mo heterostructure. The isosurfaces vividly illustrate the formation of strong electron bridges (covalent bonds) between the transition metals and Oxygen atoms across the interface, highlighting the robust p-d hybridization responsible for the material's structural and thermomechanical stability.

bond provides a high degree of thermomechanical integrity, ensuring that these RAM coatings will have superior resistance to shear stress and the risk of delamination when applied in practical environments subjected to thermal and mechanical stresses. This observation is consistent with recent DFT topological analyses of transition-metal compounds [37], [38] and engineered heterointerfaces [25], [29], which demonstrate that strong p-d orbital hybridization across oxide boundaries effectively lowers interfacial formation energy and prevents structural delamination.

3.3.3 Intrinsic ferrimagnetism and magnetic loss mechanism

The second criterion for advanced microwave-absorbing materials is magnetic attenuation capability. First-principles calculations predict that the Fe-doped Ti-Mo supercells possess a very large total magnetic moment of 17.09 μB per 180-atom supercell. The quantum mechanism underlying this giant magnetic phenomenon can be exploited through PDOS analysis of the Iron (Fe) atoms embedded in the matrix (Figure 3, green dashed curve).

There is an extreme asymmetry between the spin-up and spin-down densities in the 3d orbitals of Fe atoms, which indicates a strong exchange splitting phenomenon. The spin-up peak is clustered in the negative-energy region (-4 eV to -2 eV), while the spin-down peak is pushed far past the Fermi level. This exchange energy splitting produces a permanent local magnetic moment, which also induces the surrounding Titanium atoms.

The presence of permanent ferromagnetic or ferrimagnetic properties in this conductive matrix provides a dual-loss mechanism. In addition to the dielectric loss of Ti and Mo conduction electrons, the magnetic moment of Fe will trigger a significant magnetic loss to high-frequency electromagnetic waves. This combination makes Fe-doped Ti-Mo heterostructures theoretically very promising as a potential new-generation electromagnetic wave-absorbing material.

To decipher the spatial distribution of the giant magnetic moment of 17.09 μB in these supercells, a Löwdin charge population analysis was performed to map the local magnetic moment at each atomic site, as summarized in Table 1. The analysis results reveal a very interesting physical phenomenon. The Fe dopant atom (Atom #180) contributes a local magnetic moment of +1.55 μ_B, which is almost entirely due to electron asymmetry in the d orbital. However, structural anomalies are observed in the Oxygen atoms and transition metal atoms (Ti/Mo) located in the first coordination radius of the Fe dopant. For example, the nearest-neighbor oxygen (Atom #88) experiences a substantial spin polarization induction up to +1.46 μ_B, which originates from the p-orbital electrons. Meanwhile, the nearby transition metal atom (Atom #144) exhibits an antiparallel magnetic moment of -1.08 μ_B. It is the cumulative summation of these varying induced local moments across all 180

Applied Science and Engineering Progress, Vol. 20, No. 4, 2027, 8388

Table 1: Löwdin population analysis of valence charge and local magnetic moments for selected representative individual atoms in the Fe-Ti-Mo heterostructure.

Atom (Element)	Position in Matrix	Valence Charge (e)	Local Magnetic Moment (μ_B)	Dominant Spin Contributor
Fe (Atom #180)	Magnetic dopant	15.54	+1.55	d-orbital (+1.57)
Ti (Atom #144)	Adjacent to Fe	10.98	-1.08	d-orbital (-0.95)
Ti (Atom #4)	Bulk (Far from Fe)	12.53	+0.27	d-orbital (+0.24)
O (Atom #88)	Adjacent to Fe	6.02	+1.46	p-orbital (+1.45)
O (Atom #17)	Bulk (Far from Fe)	6.66	+0.01	p-orbital (+0.01)

(Note: The reported values represent the moment of a single atom at the specified site to illustrate the local superexchange mechanism, not the cumulative sum of all atoms in the 180-atom supercell).

atoms in the supercell that mathematically yields the total macroscopic magnetic moment of 17.09 μ_B.

In contrast to the atoms in the bulk region (away from the dopant), which have magnetic moments close to zero, the extreme polarization around Fe strongly suggests a local superexchange interaction facilitated by strong p-d hybridization. The characteristic, strongly delocalized electrons around these dopant sites create an extended spin density distribution that acts as a prominent magnetic dipole. It is the presence of this interconnected network of microscopic magnetic dipoles that, in theory, facilitates the absorption of electromagnetic waves via a highly efficient magnetic loss mechanism, underscoring the potential of this material for advanced EMI shielding and radar applications.

Furthermore, macroscopic analysis of the ground state requires a precise distinction between magnetic parameters. Here, the 'total magnetic moment' (17.09 μ_B per 180-atom supercell) represents the net spatial integral of the spin density (n_{up} - n_{down}), whereas the integrated absolute spin density (36.76 μ_B per 180-atom supercell) represents the spatial integral of the absolute value of the spin density ($|n_{up}$ - $n_{down}|$). The fact that the integrated absolute spin density is far greater than the total magnetic moment provides quantitative confirmation that the spin alignment within the lattice is not fully parallel (not pure ferromagnetic), but rather indicates a strong ferrimagnetic structure. This ferrimagnetic property, supported by antiparallel moments on transition-metal atoms around the Fe dopants (as seen in the Löwdin analysis), is crucial for microwave-absorbing applications. Materials with intrinsic ferrimagnetic order exhibit higher natural resonance frequencies and superior broadband absorption than conventional ferromagnetic materials, thereby drastically improving magnetic loss performance.

Because the 180-atom supercell utilizes a single isolated Fe dopant to accurately represent the highly dilute experimental concentration (~1.0 at%), evaluating macroscopic long-range magnetic ordering (e.g., calculating relative exchange energies between distant Fe atoms for FM vs. AFM ground states) is structurally infeasible. Therefore, this difference between total and absolute moments is strictly interpreted as robust local spin polarization characterizing an uncompensated, localized ferrimagnetic-like alignment between the Fe dopant and its immediate lattice environment rather than definitive proof of crystal-wide long-range magnetic ordering.

To comprehensively visualize the spatial distribution of the magnetic moment, a 3D spin-density contour map has been extracted and is shown in Figure 5. The mapping visually corroborates the results of the Löwdin charge analysis. It is observed that while the Fe dopant acts as the primary magnetic origin, the overall spin density (represented by the yellow and cyan isosurfaces) is highly delocalized, propagating extensively across the lower Titanium-oxide layer rather than being strictly confined to the dopant site. This visual manifestation of an extended spin density distribution bridging the transition metals and Oxygen atoms across the lattice provides a compelling theoretical representation of a long-range, p-d hybridization-driven superexchange interaction. From the perspective of practical microwave attenuation, this extensive spin delocalization is highly advantageous; it expands the effective magnetic dipole network throughout the conductive matrix, thereby maximizing the active interaction volume with external radar waves to dissipate energy via magnetic loss. Compared to previously reported single-phase Fe-doped TiO_2 systems that exhibit strictly localized magnetic moments around the dopant site [43], [44], the ternary Fe-Ti-Mo heterostructure evaluated in this work demonstrates a broader spin-polarization distribution, which is highly

Applied Science and Engineering Progress, Vol. 20, No. 4, 2027, 8388

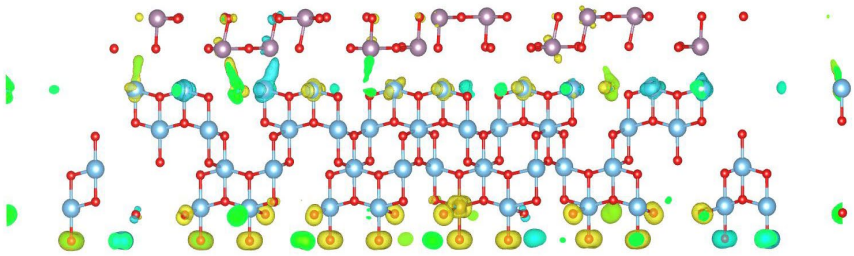


Figure 5: Three-dimensional spin density contour of the Fe-doped Ti-Mo oxide heterostructure. The distributed yellow and cyan isosurfaces visually corroborate the extensive spin delocalization across the Ti-oxide layer, highlighting the long-range p-d superexchange pathways that effectively expand the magnetic loss volume for enhanced microwave attenuation.

favorable for enhancing magnetic attenuation in oxide-based absorbers [15], [16], [24].

3.3.4 Interface polarization and work function

To quantitatively prove the occurrence of interfacial polarization and charge redistribution in Fe-doped Ti-Mo heterostructures, electrostatic potential profiles were calculated along the Z-axis plane (material thickness), as presented in Figure 6. The macroscopic average curve (red) clearly shows a strong asymmetry across the material surface.

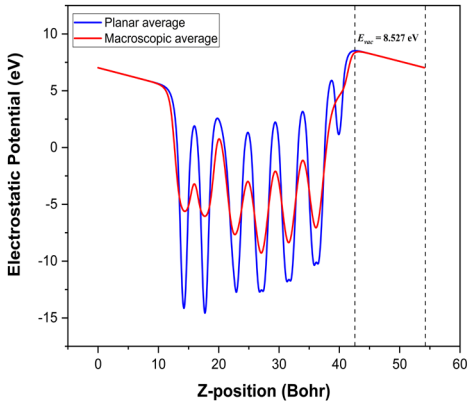


Figure 6: Planar and macroscopic average electrostatic potential of the Fe-doped Ti-Mo heterostructure along the z-direction (perpendicular to the interface). The asymmetric potential profile confirms the establishment of an internal built-in electric field, which governs the interfacial polarization mechanism.

The vacuum energy (E_{vac}) was extracted from the plateau of the macroscopic average electrostatic potential in the 15 Å vacuum region above the Molybdenum oxide-terminated surface, reaching a maximum of 8.527 eV. By correcting this against the calculated Fermi energy level (E_F = 0.3749 eV, where $\Phi = E_{vac} - E_F$), the effective macroscopic average work function (Φ) of this specific surface was evaluated to be 8.15 eV. It is well-documented in the literature that pure MoO_3 is already one of the highest-work-function oxides, typically exhibiting macroscopic values around 6.40–6.76 eV due to the strong surface dipole layer created by terminal oxygen sites [45]. The extraordinarily elevated value of 8.15 eV observed in the DFT model is attributed to a cumulative quantum-mechanical effect. First, the significant charge redistribution across the TiO_2/MoO_3 heterojunction creates a strong built-in interfacial dipole that stacks synergistically with the MoO_3 surface dipole. Secondly, the Fe dopant acts as a deep electron trap, shifting the Fermi level deeper toward the valence band, which mathematically widens the work function gap. While standard GGA-PBE calculations for highly asymmetric slabs may slightly overestimate the absolute vacuum potential, the fundamental physical implication remains robust: the extreme difference in potential height between the Ti-O and Mo-O interfaces definitively triggers the formation of a substantial built-in potential gradient.

The presence of this microscopic internal electric field drives the transfer of electron charge

Applied Science and Engineering Progress, Vol. 20, No. 4, 2027, 8388

from low- to high-potential regions, leading to charge accumulation at the heterojunction boundary. While a static electrostatic potential profile does not definitively prove dynamic macroscopic polarization, this built-in electric field acts as a fundamental thermodynamic prerequisite. Theoretically, this localized charge accumulation behaves akin to a nanocapacitor network; under an external alternating electromagnetic field (such as microwave radar), it provides the essential localized charge carriers and driving force to facilitate enhanced interfacial polarization and subsequent dielectric loss. This interfacial macroscopic polarization is further synergistically amplified at the atomic level by localized dipole moments generated from Fe-catalyzed oxygen vacancies, creating a comprehensive multi-scale dielectric loss network. Similar built-in potential gradients have been reported in recent heterostructured microwave absorbers [8], [10], [13], [14], where asymmetric work functions across phase boundaries act as the primary driving force for space-charge accumulation and dielectric relaxation.

3.3.5 d-Band center modulation and synergistic attenuation mechanism

To gain a deeper theoretical understanding of the specific contribution of each transition metal to the wave attenuation performance, the first moment of the PDOS curve is calculated to extract the value of the d-band center (ϵ_d). The distance of the d-band center(ϵ_d) relative to the Fermi level (E_F) is calculated using the normalized numerical integral equation 1:

$$\epsilon_d = \frac{\int E.\ \rho(E)\ dE}{\int \rho(E)\ dE} \quad (1)$$

where$r(E)$ is the projected density of states (PDOS). The integration was performed across the primary valence band states, with limits set from -10 eV up to the Fermi level (E_F = 0 eV). To account for the magnetic nature of the material, $r(E)$ was obtained by summing both the majority and minority spin channels. The calculated values represent the average of the equivalent transition metal atoms located specifically at the heterostructure interface to ensure a consistent environmental reference.

The calculation results confirm the existence of a structured energy hierarchy, with ϵd values of -0.48 eV, -1.71 eV, and -1.84 eV for Titanium, Iron, and Molybdenum, respectively. Titanium's d-band, which is very close to the Fermi level, indicates a high degree of electron delocalization, making it the primary channel for charge-carrier mobility and facilitating dielectric loss. In contrast, the Iron (Fe) dopant has a d-band center at an intermediate depth (-1.71 eV). This energy position is crucial; it is deep enough to prevent magnetic electrons from fully delocalizing into the conduction band, thereby maintaining the localization of permanent magnetic moments and the exchange splitting that drives magnetic loss.

On the other hand, Molybdenum has the deepest d-band (-1.84 eV), which is a manifestation of the strong p-d hybridization with Oxygen orbitals. This decrease in energy level minimizes the Pauli repulsion at the interface, thus locking the lattice structure thermodynamically. While d-band center values cannot stand alone as definitive proof of macroscopic functional roles, this calculated energy hierarchy strongly corroborates the preceding multiparameter analyses. The shallow Ti state aligns with the high charge mobility potential seen in the DOS; the intermediate Fe state supports the magnetic localization evidenced by the Löwdin and spin-density maps; and the deep Mo state correlates with the thermodynamic structural stability visualized in the ELF topology. Together, this theoretical synergy suggests a well-orchestrated interfacial architecture highly conducive to advanced electromagnetic attenuation. Such d-band center modulation aligns with recent transition-metal doping and heterointerface studies [19], [36], [44], which confirm that tuning the relative d-orbital energy levels relative to the Fermi level is a decisive factor in balancing charge-carrier transport and structural stability.

3.4 *Thermodynamic validation of Fe dopants as catalytic centers for oxygen vacancy formation*

To quantitatively validate the specific role of Fe dopants in modulating the dielectric loss properties of the Ti-Mo composite matrix, a first-principles thermodynamic evaluation based on molecular clusters (DFT/B3LYP/def2-SVP) was conducted. The key parameter evaluated is the relative energy of hydroxyl dissociation (simulating a hydrated surface vacancy) within the neutral cluster model (E_{vac}), as such localized surface defect sites drive dipole

Applied Science and Engineering Progress, Vol. 20, No. 4, 2027, 8388

formation and electron trapping, which are crucial to the mechanism of electromagnetic wave attenuation.

Comparative simulations were performed by modeling the dissociation of an oxygen species from a pristine Titanium bonding site (the host matrix) versus an Iron (Fe) dopant site. Table 2 summarizes the extracted Final Gibbs Free Energy (G) values at room temperature and the calculated Evac for both computational models.

By utilizing the pure Titanium cluster as a localized computational control, an extreme energy contrast is observed between the pristine matrix and the Fe-doped region. In the representative pure TiO_2 cluster, the dissociation of an oxygen species from the crystal lattice requires a highly endothermic energy of +3.53 eV. This high positive value indicates that the covalent Ti-O bond is thermodynamically highly stable and exhibits strong resistance to structural defect formation. Conversely, when the computational focus shifts to the coordination environment of the Fe dopant, the E_{vac} value drops sharply, reaching an exothermic value of -1.39 eV. While a negative value (-1.39 eV) in a localized cluster model does not mathematically dictate that the macroscopic solid will spontaneously decompose under ambient conditions, this extreme comparative thermodynamic transition (from +3.53 eV to -1.39 eV) provides strong theoretical evidence that the Fe dopant does not merely passively substitute in the matrix. Instead, it acts as a highly active localized catalytic center that significantly lowers the energy barrier for surface defect formation relative to the pristine matrix, facilitating targeted defect proliferation. This thermodynamic trend corroborates recent empirical and computational studies on defect-engineered TiO_2 [32] and Fe-doped MoO_3 nanostructures [41], which established that transition-metal doping facilitates vacancy generation to create localized dipole traps for enhanced electromagnetic energy dissipation [19], [22], [39].

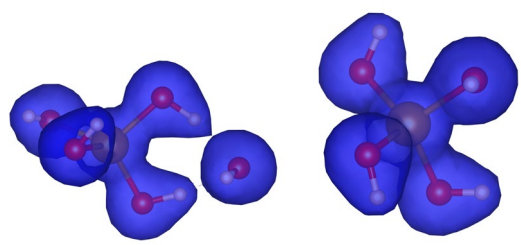
To spatially confirm this destabilization phenomenon and the formation of charge-trapping centers, topological analysis of the electron density was performed from the geometry-optimized wavefunctions (Figure 7). The visual evidence in Figure 7a corroborates the spontaneous (negative) thermodynamic value obtained in Table 2. The electron cloud on one of the hydroxyl groups appears disconnected from the primary electron density of the central Fe atom, indicating steric repulsion within the pristine cluster. This visual evidence confirms that the Fe site inherently rejects excessive oxygen coordination.

Table 2: Energy parameters for hydroxyl dissociation (surface vacancy model) in the neutral cluster models at Ti and Fe sites.

Thermodynamic Parameter	Pure Titanium Cluster Model	Fe-Doped Cluster Model
Pristine Cluster Energy ($G_{pristine}$)	-1228.1826 E_h	-1642.0877 E_h
Defective Cluster Energy (G_{defect})	-1152.4195 E_h	-1566.5054 E_h
Dissociated Hydroxyl Energy (G_{OH})	-75.6336 E_h	-75.6336 E_h
Relative Vacancy Generation Energy (E_{vac})	+3.53 eV	-1.39 eV

Note: The large negative values reported in E_h (Hartrees) represent the absolute Final Gibbs Free Energy (G), which encompasses the raw electronic energy combined with Zero-Point Energy (ZPE) and thermal/entropic corrections at 298.15 K. All reactions are strictly stoichiometrically balanced. The final cluster-based vacancy generation energy (E_{vac}) in eV is derived using the relation $E_{vac} = [G_{defect} + G_{OH} - G_{pristine}] \times 27.2114$ eV/ E_h. For instance, the Fe-doped $E_{vac} = [(-1566.5054) + (-75.6336) - (-1642.0877)] \times 27.2114 = -1.395$ eV.

Furthermore, after oxygen release, the defective cluster in Figure 7b shows a highly asymmetric charge distribution. The electrons previously participating in the Fe-O bond do not dissociate from the oxygen; instead, they delocalize and accumulate, forming a prominent electron cloud protruding into the vacuum. This cloud of delocalized electrons, strictly localized at the oxygen vacancy, definitely acts as an electron trap.



(a) (b)

Figure 7: Electron density topology visualization (isosurface level = 0.005 e/Bohr^3) for (a) the pristine Fe cluster prior to oxygen dissociation, and (b) the reduced cluster exhibiting an oxygen vacancy.

Applied Science and Engineering Progress, Vol. 20, No. 4, 2027, 8388

Macroscopically, in advanced Radar Absorbing Material (RAM) applications, when the material is exposed to high-frequency radar waves, the unpaired electrons at these trap sites respond aggressively to external electromagnetic field fluctuations. This response triggers substantial interfacial polarization. The synergistic combination of enhanced dielectric loss (driven by Fe-induced surface defects) and magnetic loss highlights the theoretical potential of the Fe-Ti-Mo heterostructure as an electromagnetic wave-absorbing material.

3.5 *Evaluation of localized moisture interaction at the defect site: A micro-solvation cluster analysis*

In practical marine applications, advanced Radar Absorbing Materials (RAM) are continuously subjected to high humidity and corrosive seawater environments. A critical failure mechanism in conventional defect-engineered RAM is "water poisoning," in which ambient H2O molecules spontaneously adsorb onto active oxygen vacancies. This parasitic adsorption annihilates the localized electron traps, drastically degrading the material's dielectric loss performance. To preliminarily evaluate localized interactions with environmental moisture, a simplified micro-solvation model using a cyclic water trimer $(H_2O)_3$ was employed. This trimer was implemented as a localized probe to examine the basic steric hindrance and local coordination stability near the defective Fe center. The energy parameters for the initial pre-reaction state and the subsequent physical adsorption attempt were extracted using DFT calculations, as summarized in Table 3.

The thermodynamic evaluation reveals a highly unfavorable interaction between the aqueous environment and the localized defect. Utilizing the standard sign convention ($E_{ads} = G_{complex}$ - å$G_{reactants}$), the calculated thermodynamic adsorption energy for the interaction between the defective Fe cluster and the $(H_2O)_3$ micro-droplet yields a substantial endothermic penalty of +2.64 eV. This extreme thermodynamic barrier explicitly dictates that the spontaneous ingress of water molecules into the oxygen vacancy is chemically prohibited under ambient conditions. This localized steric resistance is consistent with recent interfacial solvation and molecular modeling studies [34], [36], which demonstrate that tailored coordination geometries at transition-metal sites can impose substantial thermodynamic penalties against undesired molecular adsorption.

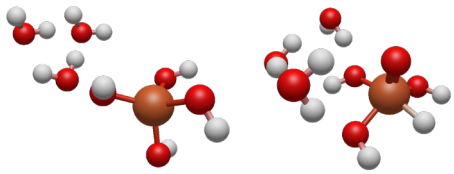
Table 3: Thermodynamic parameters for micro-solvation interaction and water-trimer adsorption at the Fe-doped vacancy site.

Thermodynamic Component	Gibbs Free Energy (*G*)
Defective Fe Cluster (G_{defect})	-1566.5054 Eh
Free Water Trimer (G_{H2O_trimer})	-228.9519 Eh
Total Initial State (G_{state1})	-1795.4573 Eh
Adsorption Complex State (G_{state2})	-1795.3603 Eh
Adsorption Energy (E_{ads})	+0.0970 Eh (+2.64 eV)

Note: The reported values represent the Final Gibbs Free Energy (G) in Hartrees (E_h), which rigorously incorporates the raw electronic energy along with Zero-Point Energy (ZPE) and thermal/entropic corrections at 298.15 K. The adsorption energy (E_{ads}) is defined using the standard thermodynamic state convention: $E_{ads} = G_{state2} - (G_{defect} + G_{H2O_trimer})$. Under this convention, a positive value indicates an endothermic (non-spontaneous) process, representing a thermodynamically unfavorable interaction rather than a kinetic activation barrier. The conversion to eV utilizes the factor 1 Eh = 27.2114 eV (i.e., +0.0970 Eh × 27.2114 eV/Eh = +2.6395 eV, reported as +2.64 eV to maintain appropriate significant figures).

Topological visualization of the modeled complex (Figure 8) elucidates the atomistic origin of this extreme endothermicity. Rather than undergoing coordinate adsorption into the vacant electron trap, the bulky $(H_2O)_3$ cluster exhibits severe steric repulsion against the host matrix. The immense steric pressure exerted by the external water droplet forces the Fe-doped site to undergo an anomalous and highly strained intramolecular surface reconstruction.

Instead of capturing the external water molecules, the severe steric repulsion from the bulky water cluster forces the central Fe atom's immediate coordination sphere into a highly distorted local energy minimum. During the structural optimization, this extreme steric strain computationally manifests as the forced cleavage of an internal O-H bond, resulting in anomalous terminal oxo (Fe=O) and metal-hydride (Fe-H) geometries. Rather than representing a proposed, kinetically viable surface reaction pathway, which would strictly require transition-state verifications, this forced structural rearrangement serves strictly to visually illustrate the severe steric resistance the active site exerts against accommodating the external micro-droplet. The +2.64 eV endothermic penalty reflects the immense energetic cost required to artificially force this spatial distortion and bond cleavage.



(a) (b)

Figure 8: Molecular visualization of the non-spontaneous interaction (E_{ads} = +2.64 eV) between the Fe-doped vacancy site and a $(H_2O)_3$ micro-droplet, illustrating severe steric repulsion and forced intramolecular surface reconstruction (formation of terminal Fe=O and Fe-H bonds).

These thermodynamic results suggest that the immediate coordination sphere around the Fe-defect exhibits noticeable local steric resistance against initial water coordination, as indicated by the calculated positive adsorption energy (+2.64 eV) and internal ligand reconstruction. However, this simplified cluster model does not replicate the complex thermodynamic environment of humid air or bulk liquid water. Definitive claims regarding macroscopic moisture resistance, wetting behavior, or long-term operational stability would require extensive multi-configuration solvation modeling and rigorous empirical testing, such as water-contact-angle measurements and humidity-aging assessments.

4 Conclusions

In this study, the rational design of an advanced microwave-absorbing material (RAM) based on a Fe-doped Ti-Mo oxide heterostructure composite has been successfully validated experimentally, and its attenuation mechanism has been elucidated using first-principles quantum-mechanical calculations. X-ray diffractogram (XRD) analysis confirmed the successful synthesis of a polycrystalline matrix incorporating layered Anatase TiO_2 and α-MoO_3 phases. The macroscopic absence of secondary iron-oxide impurity phases in the XRD profile provides an empirical baseline supporting the successful integration of Fe atoms into the host lattice, justifying the theoretically idealized substitutional model used in the DFT calculations.

A computational Density Functional Theory (DFT) approach on a large-scale 180-atom supercell provides a comprehensive understanding of the dual-loss mechanism at the interface. First, the calculated density of states of the material crosses the Fermi level, theoretically facilitating high electron mobility. This property is crucially enhanced by the asymmetry of the interlayer electrostatic potential, which peaks at a work function of 8.15 eV. This large potential gradient triggers intense interfacial charge redistribution, transforming the phase boundary into a nanocapacitor network that is highly efficient in trapping and dissipating radar waves. Secondly, the integration of Fe dopants serves as a highly active magnetic absorption center, resulting in a substantial total magnetic moment of 17.09 μB per 180-atom supercell. The large disparity between the integrated absolute spin density and the total magnetic moment, alongside the p-d hybridization-driven superexchange interactions, supports the formation of a strong intrinsic ferrimagnetic order, leading to an extensive, delocalized spin density distribution that facilitates high-frequency magnetic attenuation.

Beyond bulk properties, localized molecular-cluster modeling reveals the critical role of Fe dopants in engineering robust active defects. Thermodynamic evaluations demonstrate that Fe sites act as catalytic centers that autonomously induce spontaneous oxygen vacancies (E_{vac} = -1.39 eV), generating localized electron traps that exponentially enhance dielectric loss. Furthermore, a micro-solvation cluster model using a $(H_2O)_3$ trimer provides preliminary qualitative insight into local steric repulsion at the Fe site (+2.64 eV), highlighting the substantial endothermic penalty against immediate water coordination at the localized defect.

Culminating this analysis, the extraction of the energy hierarchy through the d-band center corroborates the findings of the multiparameter investigation: the Ti state (-0.48 eV) aligns with electron mobility potential, the Fe state (-1.71 eV) supports localized magnetic moments, and the Mo state (-1.84 eV) correlates with thermomechanical stability. This perfect balance among structural heterogeneity, interfacial capacitor polarization, local ferrimagnetism, and moisture-resistant electron traps establishes Fe-doped Ti-Mo oxide heterostructures as a highly durable blueprint for next-generation EMI shielding and robust microwave-absorbing technologies.

However, it is important to acknowledge that the conclusions drawn herein are fundamentally

Applied Science and Engineering Progress, Vol. 20, No. 4, 2027, 8388

predictive, serving as a first-principles theoretical framework derived from static atomic-level thermodynamic and electronic properties. The absence of comprehensive macroscopic empirical validations remains a limitation of this fundamental study. Future experimental investigations must address these gaps through a rigorous multiparameter approach. First, dynamic electromagnetic and magnetic performance must be empirically validated using Vector Network Analyzer (VNA) and Vibrating Sample Magnetometer (VSM) testing. Second, complete physicochemical and macroscopic structural characterizations, specifically utilizing SEM/TEM and EDS for particle morphology and exact elemental composition, Brunauer-Emmett-Teller (BET) analysis for specific surface area, TGA/DSC for thermal stability, and rigorous physical testing for coating thickness, density, and mechanical adhesion, are strictly required. Finally, conducting empirical water-contact-angle and humidity-aging tests, ensuring rigorous statistical replication of synthesis batches, and performing comprehensive comparative analyses against pure and undoped control samples are essential to definitively translate these quantum-mechanical insights into practical, device-level microwave-absorbing materials.

Author Contributions

A.F.K.W.: conceptualization, methodology, investigation, funding acquisition, writing—an original draft; writing—reviewing and editing. P.Y.: conceptualization, supervision and validation. M.S.B.: investigation, supervision and validation. M.P.: investigation, supervision and validation. All authors have read and agreed to the published version of the manuscript.

Conflicts of Interest

The authors declare no conflict of interest.

Declaration of generative AI and AI-assisted technologies in the writing process

The authors utilized the Grammarly tool to enhance the language and readability of the manuscript. The authors explicitly declare that no generative AI or AI-assisted technologies were utilized to generate data, analyze results, or create any images, figures, or graphical representations presented in this study. All theoretical models and graphical contours were rendered directly from raw computational outputs using standard scientific visualization software.

References

[1] T. Bansala, M. Joshi, and S. Mukhopadhyay, "Electromagnetic interference shielding behavior of chemically and thermally reduced graphene based multifunctional polyurethane nanocomposites: A comparative study," *Journal of Applied Polymer Science*, vol. 136, no. 25, Jul. 2019, Art. no. 47666, doi: 10.1002/app.47666.

[2] S. Mahmud, A. R. Chowdhury, S. Hannan, M. T. Islam, A. S. Alshammari, and M. S. Soliman, "Polarization-selective metamaterial absorber using tailored Y-shaped SRR for UWB device and Doppler navigation aids applications," *Heliyon*, vol. 10, no. 23, Dec. 2024, Art. no. e40102, doi: 10.1016/j.heliyon.2024.e40102.

[3] J. Jung, C. Ippolito, C. Rogers, R. Kerczewski, A. Downey, and K. Matheou, "Small unmanned aircraft electromagnetic interference (EMI) initial assessment," in *2018 Integrated Communications, Navigation, Surveillance Conference (ICNS)*, pp. 1–25, Apr. 2018, doi: 10.1109/ICNSURV.2018.8384918.

[4] U. Abubakar, S. Mekhilef, H. Mokhlis, M. Seyedmahmoudian, A. Stojcevski, and M. Rawa, "The impacts of terrestrial wind turbine's operation on telecommunication services," *Energies*, vol. 16, no. 1, 2023, Art. no. 371, doi: 10.3390/en16010371.

[5] M. Emek, E. İ. Şahin, and J. E. F. M. Ibrahim, "Production and shielding effectiveness features of chopped strands backed-$GdMnO_3$ composites for 6.5–17.5 GHz applications," *Materials*, vol. 18, no. 4, Feb. 2025, Art. no. 863, doi: 10.3390/ma18040863.

[6] Z. Zhang, M. Yang, Y. Zhang, and M. Zhou, "Research and application of terahertz response mechanism of few-layer borophene," *Nanomaterials*, vol. 12, no. 15, Aug. 2022, Art. no. 2702, doi: 10.3390/nano12152702.

[7] X. Chen, W. Wang, R. Su, Y. Huang, Y. Li, and R. He, "3D-printed electromagnetic microwave

absorption structures: A comprehensive review," *Journal of Materials Chemistry A*, vol. 13, no. 28, pp. 22240–22270, Jul. 2025, doi: 10.1039/D5TA02073E.

[8] M. He et al., "Low-frequency microwave absorption composites," *Advanced Science*, vol. 12, no. 35, Sep. 2025, Art. no. e11580, doi: 10.1002/advs.202511580.

[9] Z. Lu et al., "Progress in electromagnetic wave absorption of multifunctional structured metamaterials," *Polymers*, vol. 17, no. 18, Sep. 2025, Art. no. 2559, doi: 10.3390/polym17182559.

[10] J. Du, T. Li, Z. Xu, J. Tang, Q. Qi, and F. Meng, "Structure–activity relationship in microstructure design for electromagnetic wave absorption applications," *Small Structures*, vol. 4, no. 11, Nov. 2023, Art. no. 2300152, doi: 10.1002/sstr.202300152.

[11] A. Parveen et al., "A review on advancing electromagnetic wave absorption in metamaterials: Progress, challenges, theoretical background, and advanced technological applications," *Advanced Materials Technologies*, vol. 10, no. 20, Oct. 2025, Art. no. e00710, doi: 10.1002/admt.202500710.

[12] J. Cheng et al., "Emerging materials and designs for low- and multi-band electromagnetic wave absorbers: The search for dielectric and magnetic synergy?," *Advanced Functional Materials*, vol. 32, no. 23, Jun. 2022, Art. no. 2200123, doi: 10.1002/adfm.202200123.

[13] G. Yu, G. Shao, R. Xu, Y. Chen, X. Zhu, and X. Huang, "Metal–organic framework-manipulated dielectric genes inside silicon carbonitride toward tunable electromagnetic wave absorption," *Small*, vol. 19, no. 46, Nov. 2023, Art. no. 2304694, doi: 10.1002/smll.202304694.

[14] Q. Zhang, J. Cui, S. Zhao, G. Zhang, A. Gao, and Y. Yan, "Development of electromagnetic-wave-shielding polyvinylidene fluoride–Ti_3C_2Tx MXene–carbon nanotube composites by improving impedance matching and conductivity," *Nanomaterials*, vol. 13, no. 3, Jan. 2023, Art. no. 417, doi: 10.3390/nano13030417.

[15] L. Wang et al., "Electromagnetic absorption by magnetic oxide nanomaterials: A review," *ACS Applied Nano Materials*, vol. 6, no. 24, pp. 22611–22634, Dec. 2023, doi: 10.1021/acsanm.3c05054.

[16] M. Wu, H. Wang, X. Liang, and D. Wang, "Flower-like 1T/2H-MoS_2@α-Fe_2O_3 with enhanced electromagnetic wave absorption capabilities in the low frequency range," *Journal of Materials Chemistry C*, vol. 11, no. 8, pp. 2897–2910, Feb. 2023, doi: 10.1039/D2TC04817E.

[17] J. Ma, J. Wang, X. Hu, L. Wang, Y. Fan, and W. Jiang, "Construction of plate-like magnetic heterostructure for synergistic microwave absorption," *Journal of the American Ceramic Society*, vol. 106, no. 1, pp. 410–419, Jan. 2023, doi: 10.1111/jace.18742.

[18] Q. Li et al., "Recent progress and outlook on the emerging low-dimensional MoS_2 nanostructures for microwave absorption," *ACS Applied Electronic Materials*, vol. 6, no. 1, pp. 120–143, Jan. 2024, doi: 10.1021/acsaelm.3c01335.

[19] A. Gaur, J. Sharma, and H. Han, "Hydrogen spillover effect in electrocatalysis: Delving into the mysteries of the atomic migration," *Energy & Environmental Materials*, vol. 7, no. 5, Sep. 2024, Art. no. e12761, doi: 10.1002/eem2.12761.

[20] P. Zhang, L. Yue, Q. Liang, H. Gao, Q. Yan, and L. Wang, "A review of transition metal compounds as functional separators for lithium-sulfur batteries," *ChemistrySelect*, vol. 8, no. 1, Jan. 2023, Art. no. 202203352, doi: 10.1002/slct.202203352.

[21] J. Wu, J. Du, X. He, and X. Guo, "Preparation of heterojunction catalysts for photocatalysis by in-situ synthesis: What we should do next?" *ChemCatChem*, vol. 16, no. 7, Apr. 2024, Art. no. e202301234, doi: 10.1002/cctc.202301234.

[22] D. Dewantara et al., "Beyond UV: Overcoming the optical bottleneck in photodesulfurization of diesel oil via visible and red-light harvesting," *Journal of Fluorescence*, vol. 36, no. 6, pp. 4213–4232, Jun. 2026, doi: 10.1007/s10895-026-04832-2.

[23] A. Hamisu, U. I. Gaya, and A. H. Abdullah, "Bi-template assisted sol-gel synthesis of photocatalytically-active mesoporous anatase TiO_2 nanoparticles," *Applied Science and Engineering Progress*, vol. 14, no. 3, pp. 313-327, Apr. 2021, doi: 10.14416/j.asep.2021.04.003.

[24] L. Trisnaliani, S. Haryati, and M. D. Bustan, "Rapid microwave method to enhance the characteristics of Fe_3O_4 and Fe_3O_4/SiO_2

nanoparticles," *Applied Science and Engineering Progress*, vol. 17, no. 3, Jun. 2024, Art. no. 7414, doi: 10.14416/j.asep.2024.06.010.

[25] S. A. Ali and T. Ahmad, "Decorating thermodynamically stable (101) facets of TiO_2 with MoO_3 for multifunctional sustainable hydrogen energy and ammonia gas sensing applications," *Inorganic Chemistry*, vol. 63, no. 1, pp. 304–315, Jan. 2024, doi: 10.1021/acs.inorgchem.3c03176.

[26] S. Li and K. Bachagha, "Application of buffer layer to improve the efficiency of organic solar cells," *Energy Technology*, vol. 12, no. 2, Feb. 2024, Art. no. 2300822, doi: 10.1002/ente.202300822.

[27] B. Ezhilmaran, S. M. Rekha, and S. V. Bhat, "Bilayer boost to UV assisted supercapacitors: Enhanced performance with transparent TiO_2/MoO_3 heterojunction electrode," *Batteries & Supercaps*, vol. 8, no. 1, Jan. 2025, Art. no. e202400654, doi: 10.1002/batt.202400654.

[28] S. Pavalamalar, M. K. K. Poojha, R. Silambarasan, U. S. S. S. Perisetti, and K. Anbalagan, "Harnessing MoO_3/TiO_2 nanocomposites for photocatalytic reduction of [Cu(dien)(1-MeIm)Cl]Cl complex: Paving the way for blue LED application," *Journal of Inorganic and Organometallic Polymers and Materials*, vol. 34, no. 5, pp. 1957–1976, May 2024, doi: 10.1007/s10904-023-02940-1.

[29] W. Li et al., "Chemical heterointerface engineering on hybrid electrode materials for electrochemical energy storage," *Small Methods*, vol. 5, no. 8, Aug. 2021, Art. no. 2100444, doi: 10.1002/smtd.202100444.

[30] D. Scirè et al., "Density of states characterization of TiO_2 films deposited by pulsed laser deposition for heterojunction solar cells," *Nano Research*, vol. 15, no. 5, pp. 4048–4057, May 2022, doi: 10.1007/s12274-021-3985-8.

[31] G. Kaur, K. Pubby, S. Bahel, and S. B. Narang, "Li_2O-Ta_2O_5-TiO_2 M-phase solid solutions as effective X-band shielders," *Ceramics International*, vol. 44, no. 16, pp. 20484–20489, Nov. 2018, doi: 10.1016/j.ceramint.2018.08.044.

[32] S. Liu et al., "Tuning oxygen vacancy concentration in defect-engineered black TiO2 nanomaterials for synergistically enhanced microwave absorption performance," *ACS Applied Nano Materials*, vol. 8, no. 45, pp. 21938–21947, Nov. 2025, doi: 10.1021/acsanm.5c03969.

[33] M. H. Samat, A. M. M. Ali, M. F. M. Taib, O. H. Hassan, and M. Z. A. Yahya, "Structural and electronic properties of TiO_2 polymorphs with effective on-site coulomb repulsion term: DFT+U approaches," *Materials Today: Proceedings*, vol. 17, pp. 472–483, 2019, doi: 10.1016/j.matpr.2019.06.482.

[34] K. Pal, N. Asthana, A. Srivastava, A. Malik, and A. A. Khan, "Computational analysis of MOF-functionalized polymeric membranes for wastewater treatment and applications," *Journal of Molecular Liquids*, vol. 405, Jul. 2024, Art. no. 125013, doi: 10.1016/j.molliq.2024.125013.

[35] J. León-Flores, M. Romero, J. Rosas-Huerta, and R. Escamilla, "Ab initio study of the crystal structure and the elastic properties of the Mo0.85Nb0.15B3 compound under pressure," *MRS Advances*, vol. 4, no. 63, pp. 3453–3461, Dec. 2019, doi: 10.1557/adv.2019.420.

[36] A. S. Kale and G. Raabe, "Developing interface force fields for water and oxygen on Pt, and Pt_3Ni, Pt_3Co alloy surfaces for proton-exchange membrane fuel cell (PEMFC) applications," *ACS Omega*, vol. 11, no. 6, pp. 10649–10663, Feb. 2026, doi: 10.1021/acsomega.5c11427.

[37] B. O. Mnisi, "Density functional theory study on structural, mechanical, electronic, and phonon properties of CrAlB, MoAlB, WAlB, CrAlGa, MoAlGa, and WAlGa ternary compounds," *The European Physical Journal B*, vol. 98, no. 3, Mar. 2025, Art. no. 42, doi: 10.1140/epjb/s10051-025-00876-8.

[38] M. Michalski, A. J. Gordon, and S. Berski, "Topological analysis of the electron localisation function (ELF) applied to the electronic structure of oxaziridine: The nature of N-O bond," *Structural Chemistry*, vol. 30, no. 6, pp. 2181–2189, Dec. 2019, doi: 10.1007/s11224-019-01407-9.

[39] D. Dewantara, I. Ismail, M. D. Bustan, and S. Haryati, "Role of tin metal in red visible light in diesel oil desulfurization process with looping process system," *Applied Science and Engineering Progress*, vol. 18, no. 4, Jan. 2025, Art. no. 7711, doi: 10.14416/j.asep.2025.01.006.

[40] A. E. Awadallah, A. A. Aboul-Enein, N. M. Yousif, M. A. Azab, and A. M. Haggar, "Plastic

waste-derived carbon nanotubes decorated with Mo_2C, MoO_3, or MoO_3/Mo_2C as effective nanocomposite materials for supercapacitor applications," *ChemistrySelect*, vol. 10, no. 17, May 2025, Art. no. 202500750, doi: 10.1002/slct.202500750.

[41] J. Li et al., "Conductometric triethylamine sensor based on Pd nanoparticles modified Fe doped MoO_3 porous nanobelts," *Sensors and Actuators B: Chemical*, vol. 429, Apr. 2025, Art. no. 137289, doi: 10.1016/j.snb.2025.137289.

[42] N. Yaacob, A. F. Ismail, G. P. Sean, and N. A. M. Nazri, "Structural and photocatalytic properties of co-doped hybrid ZrO_2–TiO_2 photocatalysts," *SN Applied Sciences*, vol. 1, no. 3, Mar. 2019, Art. no. 252, doi: 10.1007/s42452-019-0247-4.

[43] W. B. Begna, G. S. Gurmesa, Q. Zhang, and C. A. Geffe, "A DFT+U study of site dependent Fe-doped TiO_2 diluted magnetic semiconductor material: Room-temperature ferromagnetism and improved semiconducting properties," *AIP Advances*, vol. 12, no. 2, Feb. 2022, Art. no. 025002, doi: 10.1063/5.0075253.

[44] V. Mishra, S. Pandey, S. Ganguly, and A. Shukla, "Engineering the electronic structure of TiO_2 by transition-metal doping: A first-principles DFT study," *Journal of Applied Physics*, vol. 138, no. 12, Sep. 2025, Art. no. 125701, doi: 10.1063/5.0280646.

[45] Y. Guo and J. Robertson, "Origin of the high work function and high conductivity of MoO_3," *Applied Physics Letters*, vol. 105, no. 22, Dec. 2014, Art. no. 222110, doi: 10.1063/1.4903538.